

1 **Comparisons of the tropospheric specific humidity from GPS radio occultations with**
2 **ERA-Interim, NASA MERRA and AIRS data**

3

4 Panagiotis Vergados¹, Anthony J. Mannucci¹, Chi O. Ao¹, Olga Verkhoglyadova¹, and Byron
5 Iijima¹

6

7 ¹ Jet Propulsion Laboratory, California Institute of Technology, Pasadena, California, USA

8

9 **Corresponding author:** P. Vergados, Jet Propulsion Laboratory, M/S 138-310B, 4800 Oak
10 Grove Dr., Pasadena, CA, 91109, USA. (Panagiotis.Vergados@jpl.nasa.gov)

11

12

13

14

15

16

17

18

19

20

21 **Abstract.** We construct a 9-year data record (2007-2015) of the tropospheric specific humidity
22 using Global Positioning System radio occultation (GPS RO) observations from the
23 Constellation Observing System for Meteorology, Ionosphere, and Climate (COSMIC) mission.
24 This record covers the $\pm 40^\circ$ latitude belt and includes estimates of the zonally averaged monthly
25 mean specific humidity from 700 hPa up to 400 hPa. It includes three major climate zones: a) the
26 deep tropics ($\pm 15^\circ$), b) the trade winds belts ($\pm 15-30^\circ$), and c) the subtropics ($\pm 30-40^\circ$). We find
27 that the RO observations agree very well with the European Center for Medium-range Weather
28 Forecasts Re-Analysis Interim (ERA-Interim), the Modern-Era Retrospective analysis for
29 Research and Applications (MERRA), and the Atmospheric Infrared Sounder (AIRS) by
30 capturing similar magnitudes and patterns of variability in the monthly zonal mean specific
31 humidity and interannual anomaly over annual and interannual timescales. [The JPL and UCAR
32 specific humidity climatologies differ by less than 15% (depending on location and pressure
33 level), primarily due to differences in the retrieved refractivity]. In the middle-to-upper
34 troposphere, in all climate zones, JPL is the wettest of all data sets, AIRS is the driest of all data
35 sets, and UCAR, ERA-Interim, and MERRA are in very good agreement lying in between the
36 JPL and AIRS climatologies. In the lower-to-middle troposphere, we present a complex behavior
37 of discrepancies, and we speculate that this might be due convection and entrainment.
38 Conclusively, the RO observations could potentially be used as a climate variable, but more
39 thorough analysis is required to assess the structural uncertainty between centers and its origin.

Comment [1]:

Reviewer #1. General Comment #2.

Addressed and completed.

44 **1 Introduction**

45 The Intergovernmental Panel on Climate Change (IPCC) Fifth Assessment Report (AR5)
46 [Flato *et al.*, 2013] reported that identifying the vertical structure of humidity is subject to great
47 uncertainty, because dynamical processes that cannot be captured by one sensor alone drive
48 water vapor. Hence, we ought to quantify and understand the degree of agreement of the water
49 vapor concentration throughout the vertical extent of in the troposphere among different sensors,
50 in order to improve the representation of the Earth’s atmospheric humidity content that is key to
51 predicting future climate [Hegerl *et al.*, 2015].

52 To-date, ground- and space-based platforms, reanalyses, and model simulations do not
53 provide precise knowledge of the water vapor’s concentration, or its trends over time, in multiple
54 regions of the Earth’s atmosphere [Sherwood *et al.*, 2010]. This is because of a combination of
55 different reasons that include: (a) sampling bias due to cloudiness, deep convection, or surface
56 emissivity variations; (b) biases due to limited local time coverage, or random observations
57 versus volume-filling scans; (c) coarse spatial resolution, and (d) misrepresentation of the
58 planetary boundary layer’s (PBL) moisture content [Hannay *et al.*, 2009] that induces errors in
59 the lower-to-middle troposphere moist convection.

60 In particular, infrared (IR) space-based platforms have a relatively coarse vertical
61 resolution (e.g., 2.0–3.0 km), are prone to cloud contamination [Fetzer *et al.*, 2006], and tend to
62 be biased low over wet and dry humidity extremes [Fetzer *et al.*, 2008; Chou *et al.*, 2009]. The
63 use of IR observations in the lower troposphere still remains a challenge, due to the decreasing
64 information content and the difficulty of detecting low-cloud contamination [Schreier *et al.*,
65 2014]. Space-based microwave (MW) limb sounders, despite having low sensitivity to
66 precipitation and clouds, have a coarse vertical resolution (e.g., 3.0 km in case of the Microwave

Comment [2]:
Reviewer #2. Minor Comment #2.
Addressed and completed.

67 Limb Sounder (MLS) [Waters et al., 2006]) and are sensitive to the a-priori solution that could
68 cause unsuccessful limb-viewing radiance retrievals (e.g., of up to 30% in the case of MLS
69 [Read et al., 2007]) under clear sky but moist conditions. Heavy cloudiness, especially in the
70 middle-to-upper troposphere can also introduce biases in the upwelling MW radiation from water
71 vapor due to the presence of ice particles that can contaminate the MW retrievals [Fetzer et al.,
72 2008]. Global Circulation Models (GCMs) do not properly represent the middle troposphere
73 moist convection [Sherwood et al., 2004; Holloway and Neelin, 2009; Frenkel et al., 2012], and
74 large discrepancies in the tropospheric humidity among different reanalyses [Chen et al., 2008]
75 and among reanalyses, models, and satellite observations [Chuang et al., 2010; Jiang et al.,
76 2012; Tian et al., 2013; Wang and Su, 2013] still persist.

77 The path towards constraining the models, reanalyses, and satellite water vapor
78 observational uncertainties is to compare them against data sets that are as independent from
79 their a-priori information as possible. Here, we use the multi-year observational record from
80 Global Positioning System Radio Occultation (GPS RO) observations as such a data set, offering
81 all-weather sensing, high vertical resolution (100–200 m; Kursinski et al. [2000]; Schmidt et al.
82 [2005]), high specific humidity accuracy (< 1.0 g/Kg), and full diurnal cycle sampling (depending
83 on the orbit and number of the RO spacecrafts).]

84 Our primary objective is to create a short-term specific humidity data record (9 years)
85 based on RO observations and compare it against NASA’s Modern Era Retrospective Analysis
86 for Research and Applications (MERRA), the European Center for Medium-range Weather
87 Forecasts Reanalysis Interim (ERA-Interim), and Atmospheric Infrared Sounder (AIRS) data
88 sets. Our goal is to evaluate the consistency of the RO specific humidity retrievals with respect to
89 state-of-the-art reanalyses and satellite observations by quantifying the RO differences with the

Comment [3]:

Reviewer #2. Minor Comment #3.

Addressed and completed.

90 rest of the data sets over the tropics and subtropics. We anticipate gaining new insights about the
91 specific humidity distribution over different convective regions, which could provide guidelines
92 for future model improvements. The uniqueness of this investigation is that this is the first study
93 to compare nearly a decade long data record of RO specific humidity information and their
94 interannual variability against MERRA, ERA-Interim, and AIRS. The description of the
95 humidity retrieval process from RO observations is discussed in detail in *Kursinski et al.* [1997],
96 *Kursinski and Hajj* [2001], and *Collard and Healey* [2003]. Of importance is the fact that we use
97 MERRA, instead of MERRA-2, because MERRA does not assimilate ROs (unlike ERA-
98 Interim), providing an independent data set when comparing the RO specific humidity
99 observations.

100 Section 2 presents the data sets we use in this analysis together with their retrieval
101 characteristics. In Section 3, we present and discuss the RO specific humidity climatologies with
102 respect to the rest of the data sets and Section 4 summarizes our current research.

103

104 **2 Methodology**

105 We create time series of tropospheric specific humidity climatologies using the COSMIC
106 observations (both the UCAR and the JPL retrievals), the MERRA and ERA-Interim data sets,
107 and the Atmospheric Infrared Sounder (AIRS) observations. These climatologies contain a 9-
108 year measurement record from January 2007 until December 2015 and represent monthly zonal
109 mean averages. We study the geographic region between $\pm 40^\circ$ latitude, which we divide into
110 three distinct dynamical regions: a) the deep tropics ($\pm 15^\circ$), b) the middle tropics ($\pm 15^\circ - 30^\circ$), and
111 c) the subtropics ($\pm 30^\circ - 40^\circ$). In each region, we study the annual and interannual variability and
112 trend of the specific humidity from all data sets, and then we quantify the mean differences and

113 standard deviations of all climatologies with respect to the JPL climatology (that we use as a
114 reference). The time series represent monthly zonal averages of the specific humidity at
115 individual pressure levels from the lower to the middle troposphere: 700 hPa, 600 hPa, 500 hPa,
116 and 400 hPa.

117 We are particularly interested in investigating the performance of the RO specific
118 humidity climatologies with respect to other databases within $\pm 40^\circ$ latitude, as it is a key region
119 for climate research [IPCC, 2007], and because models and observations exhibit large
120 differences in the middle and upper troposphere in this band [e.g., Jiang et al., 2012; Tian et al.,
121 2013; Wang and Su, 2013]. We focus between 700 hPa and 400 hPa, because although tracking
122 of the GPS signals in the lower troposphere (e.g., below 700 hPa) has been greatly improved
123 with the use of open loop tracking techniques [Sokolovskiy et al., 2006], the presence of the
124 water vapor and small signal-to-noise ratio could still cause loss of lock for lower altitudes.
125 Additionally, atmospheric ducting at and below the planetary boundary layer could also lead to
126 negative refractivity biases [Ao et al., 2003; Xie et al., 2010]. Above 400 hPa, the signature of
127 water vapor on the atmospheric refractivity is small, leading to larger retrieval errors.

128

129 2.1 Constellation Observing System for Meteorology, Ionosphere and Climate

130 The COSMIC constellation of six microsattellites were launched in April 2006 orbiting
131 the Earth at an altitude of ~ 800 km in near-circular Low Earth Orbit (LEO) [Anthes et al., 2008].
132 They measure the phase and amplitude of the transmitted dual frequency L -band GPS signals
133 ($f_1=1.57542$ GHz; $f_2=1.22760$ GHz) as a function of time. The relative motion of the COSMIC
134 satellites with respect to the GPS satellites and the presence of the atmosphere cause a Doppler
135 frequency shift on the transmitted GPS signals received by the COSMIC satellites. The

Comment [4]:

Reviewer #1. Specific Comment #4.

Reviewer #2. Minor Comment #5.

Addressed and completed.

136 magnitude of the Doppler frequency shift is estimated as the time derivative of the recorded GPS
137 signal phases, which together with precise knowledge of the position and velocity information of
138 both the COSMIC and the GPS satellites allows for estimation of the amount of bending of the
139 transmitted GPS signals due to the presence of the atmosphere, from which one can infer the air
140 refractive index [Kursinski *et al.*, 1997]. In the lower troposphere, the bending angle is retrieved
141 using radioholographic methods (such as canonical transform or full spectrum inversion) that
142 eliminate errors due to atmospheric multipath [e.g., *Ao et al.*, 2003]. The relative motion of the
143 COSMIC and GPS satellite pair allows for the vertical scanning of the atmosphere providing
144 vertical profiles of atmospheric refractivity, which contain temperature and humidity
145 information.

146 We use RO-derived specific humidity products from both the UCAR and the JPL
147 processing centers, which follow different processing techniques. Although this study does not
148 focus on these differences, we note that UCAR adopts a variational assimilation method, which
149 requires *a-priori* estimates of the atmospheric water vapor content (provided by ERA-Interim),
150 implying that the derived specific humidity products may be subject to the error characteristics of
151 the humidity initialization. On the other hand, JPL uses the refractivity equation (along with the
152 hydrostatic equation and equation of state) to estimate the water vapor pressure given *a-priori*
153 knowledge of air temperature [Hajj *et al.*, 2002]:

$$N = 77.6 \frac{P}{T} + 3.73 \cdot 10^5 \frac{e}{T^2} \Leftrightarrow e = \frac{1}{3.73 \cdot 10^5} (NT^2 - 77.6PT) \quad [1]$$

154
155
156 Where N (unitless) is the refractivity, P (mbar) is the pressure, T (K) is the temperature, and e
157 (mbar) is the RO-derived water vapor pressure. The equation we use to convert the water vapor

Comment [5]:
Reviewer #2. Minor Comment #6.
Addressed and completed.

Comment [6]:
Reviewer #1. General Comment #2.
Addressed and completed.

158 pressure into specific humidity is given by:

159

$$q = 621.9907 \cdot \frac{e}{(P - e)} \quad [2]$$

160

161 Where q (g kg^{-1}) is the specific humidity, P (mbar) is the pressure, and e (mbar) is the RO-

162 derived water vapor pressure. The retrieval errors of the JPL SH products do not contain *a-priori*

163 humidity information, but are subject to errors in the *a-priori* temperature information, which is

164 provided by the ECMWF Tropical Ocean and Global Atmosphere (TOGA) database. Because

165 Eq. (1) requires that both the RO and the ECMWF TOGA data sets be reported at the same

166 pressure levels, we interpolate the temperature profiles into the vertical grid of the RO profiles

167 using linear interpolation in the log pressure domain. Currently, the JPL-retrieved COSMIC ~~air~~

168 refractivity profiles are provided at 200 m vertical resolution in the lower to middle troposphere.

169

170 2.2 Modern-Era Retrospective Analysis for Research and Application

171 We use the MERRA (v5.2.0) analysis that employs a 3-D variational assimilation

172 technique based on the Gridpoint Statistical Interpolation (GIS) scheme with a 6-hour update

173 cycle [e.g., *Wu et al.*, 2002]. It did not yet assimilate RO observations, and therefore, it is an

174 independent dataset from COSMIC. Besides MERRA-2 assimilating GPS RO bending angle

175 observations, it also includes significant changes with respect to MERRA in regards to moisture

176 analysis that have a direct affect on the water cycle [*Gelaro et al.*, 2016; *Takacs et al.*, 2016;

177 *Bosilovich et al.*, 2017]. Although GPS RO comparisons with MERRA-2 could provide valuable

178 statistics, they would not represent a clear picture of the effect of assimilating GPS RO

179 observations, unless the impact of all other improvements on the humidity climatology is first

Comment [7]:

Reviewer #2. Minor Comment #7.

Addressed and completed.

Comment [8]:

Reviewer #1. Specific Comment #6.

Addressed and completed.

Comment [9]:

Reviewer #2. Minor Comment #8.

Addressed and completed.

180 | **determined.** We analyze the monthly gridded specific humidity products given in a 1/2-degree x
181 | 2/3-degree latitude–longitude grid and 42 vertical pressure levels. In the troposphere, the vertical
182 | pressure resolution from the surface up to 700 hPa is 25 hPa, whereas from 700 hPa until 300
183 | hPa the vertical resolution is 50 hPa. MERRA is a NASA analysis that assimilates satellite
184 | observations using Goddard’s Earth Observing System (GOES) version 5.2.0 Data Assimilation
185 | System (DAS) [Rienecker *et al.*, 2008]. Primarily, it assimilates radiances from AIRS, the
186 | Advanced Television and Infrared Observatory Spacecraft Operational Vertical Sounder
187 | (ATOVS), and the Special Sensor Microwave Imager (SSM/I), and figure 4 in Rienecker *et al.*
188 | [2011] provides a detailed list of the rest of the data sets that are assimilated.

Comment [10]:

Reviewer #2. Minor Comment #4.

Addressed and completed.

189

190 **2.3. European Center for Medium-Range Weather Forecasts Re-Analysis Interim**

191 | We use the ERA-Interim [Dee *et al.*, 2011], which uses a 4-D variational assimilation
192 | technique [Simmons *et al.*, 2005] to analyze a variety of observational data sets to predict the
193 | state of the atmosphere with accuracy similar to what is theoretically possible based on the error
194 | characteristics of the assimilated data [Simmons and Hollingsworth, 2002]. We analyze the
195 | monthly gridded SH products given in a 0.75 degree x 0.75 degree latitude-longitude grid and 20
196 | pressure levels from 1000 hPa up to 300 hPa. The vertical resolution from the surface up to 750
197 | hPa is 25 hPa, but the vertical resolution decreases to 50 hPa between 750 hPa and 300 hPa. The
198 | primary data sets assimilated in ERA-Interim are radiosonde humidity observations, AIRS and
199 | microwave radiances, and as of November 2006, the GPS RO bending angle profiles.

200

201 **2.4. Atmospheric Infrared Sounder**

202 | We use the AIRS/AMSU v6 Level-3 data [Tian *et al.*, 2013a] and analyze the monthly

203 gridded SH product given in a 1-degree x 1-degree latitude-longitude grid, which extend from
204 the surface up to 100 hPa in 12 vertical pressure levels (~ 2.0 km vertical resolution). The latest
205 AIRS v6 SH products are now available at standard pressure levels. The vertical resolution
206 between the surface up to 850 hPa is 75 hPa; between 700 hPa and 300 hPa the vertical
207 resolution decreases to 100 hPa, and above the 300 hPa pressure level up to 100 hPa the vertical
208 resolution is 50 hPa. The AIRS physical retrievals use an IR–microwave neural net solution
209 [Blackwell *et al.*, 2008] as the first guess for temperature and water vapor profiles based on
210 MIT’s stochastic cloud-clearing and neural network solution described in Khan *et al.* [2014].

211

212 2.5. Establishing Data Set Accuracy

213 *Kursinski et al.* [1995] estimated that occultation water vapor pressure profiles at the
214 tropics have a precision between 10 and 20% below 7.0 km altitude assuming temperature errors
215 of 1.5 K, surface pressure errors of 3 mbar, and refractivity errors of < 0.2%, which translate to a
216 specific humidity precision of < 0.25 g kg⁻¹ at 700 hPa and < 0.03 g kg⁻¹ at 400 hPa, given a
217 mean specific humidity of 4.0 g kg⁻¹ at 700 hPa and 1.0 g kg⁻¹ at 400 hPa between 01/2007 and
218 21/2015. *Kursinski and Hajj* [2001] determined that the precision of individual occultation
219 specific humidity profiles is ~0.20–0.50 g kg⁻¹ in the middle-to-lower troposphere. *Ho et al.*
220 [2007] combined AIRS and RO data retrieving specific humidity profiles in the lower
221 troposphere with root-mean-square-error (RMSE) between 0.40 g kg⁻¹ (at 700 hPa) and 0.05 g
222 kg⁻¹ (at 400 hPa). *Ho et al.*, [2010] collocated RO and ECMWF profiles near radiosonde
223 locations and estimated that the standard deviation of the differences between the two data sets is
224 < 0.50 g kg⁻¹ above 3.0 km altitude. *Kishore et al.*, [2011] estimated that the differences between
225 the ERA-Interim and COSMIC are -0.15±0.22 g kg⁻¹ at 3.0 km and -0.07±0.06 g kg⁻¹ at 7.0 km,

226 in the deep tropics ($\pm 20^\circ$). They also estimated that the differences between the Japanese Re-
227 Analysis 25-year (JRA-25) and COSMIC are about $-0.10 \pm 0.23 \text{ g kg}^{-1}$ at 3.0 km and $-0.20 \pm 0.06 \text{ g}$
228 kg^{-1} at 7.0 km. *Ao et al.* [2012] estimated that the specific humidity precision is $\sim 0.15 \text{ g kg}^{-1}$ per
229 degree kelvin error in temperature. *Vergados et al.* [2014] reported that RO specific humidity is
230 retrieved within $\sim 0.20\text{--}0.40 \text{ g kg}^{-1}$ accuracy at the tropics, provided the RO refractivity accuracy
231 is $\sim 1.0\%$ at an altitude of 2.0 km decreasing to $\sim 0.2\%$ at an altitude of 8.0 km [*Kuo et al.*, 2005]
232 and a temperature error of $\pm 1.0 \text{ K}$. Recently, *Kursinski and Gebhardt* [2014] proposed a novel
233 approach to further improve the retrieved humidity accuracy and precision from RO observations
234 in the middle troposphere.

235 Conclusively, the specific humidity accuracy and precision from RO observations
236 depends on altitude and we determine it to be $\sim 10\text{--}20\%$. MERRA assimilates various
237 observational data sets and the SH accuracy is a function of the accuracy of the assimilated
238 products. In general, the MERRA specific humidity retrievals are accurate to $\sim 20\%$ [*Rienecker et*
239 *al.*, 2011]. AIRS estimated specific humidity product accuracies are typically $\sim 25\%$ at $p > 200$
240 hPa [*Fetzer et al.*, 2008], and ERA-Interim specific humidity products have an estimated
241 accuracy of $\sim 7\text{--}20\%$ in the tropical lower-to-middle troposphere [*Dee et al.*, 2011]. The RO
242 retrievals seem to have better accuracy than the AIRS retrievals, which could be attributed to the
243 fact that the RO observations are based on precise time measurements and have very low
244 sensitivity to clouds (unlike the IR observations). In general, the RO observations seem to have
245 similar accuracy and precision with both the MERRA and ERA-Interim reanalyses.

247 3. Results and Discussion

248 3.1. Analysis of the specific humidity in the deep tropics

Comment [11]:

Reviewer #2. Minor Comment #11.

Addressed and completed.

Comment [12]:

Reviewer #1. General Comment #3.

Addressed and completed.

Comment [13]:

Reviewer #1. Specific Comment #3.

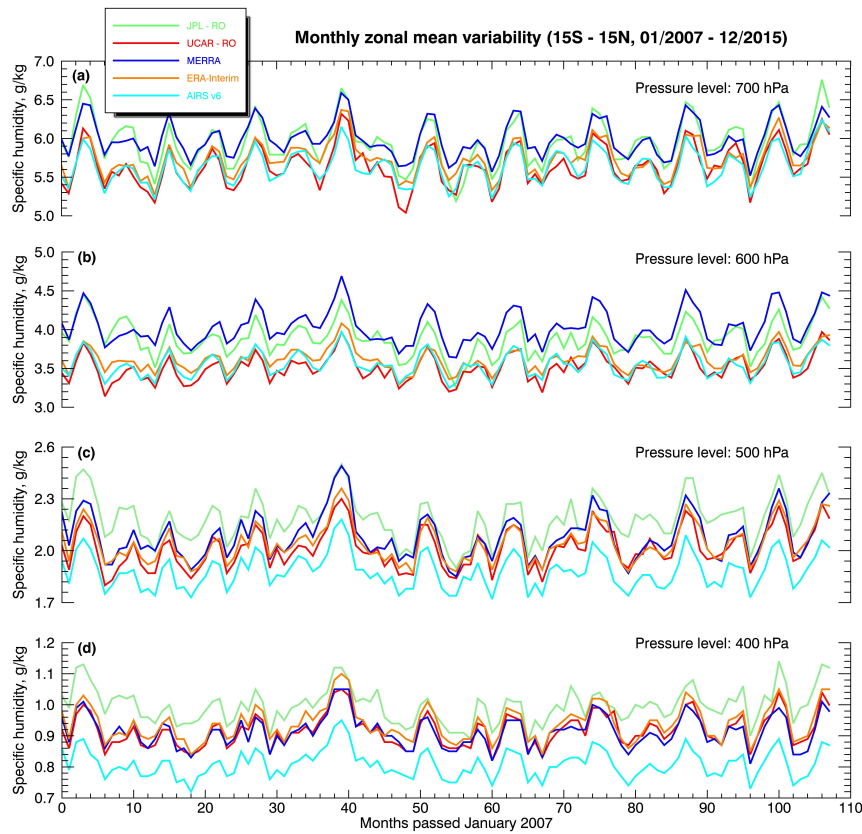
Addressed and completed.

Comment [14]:

Note: We deleted this text, because we have already mentioned this details in the Methodology Section.

Deleted: We divide this section into three sub-sections that represent the three tropical climate environments we analyze, each of which exhibits different atmospheric dynamic properties. In each sub-section, we study the long-term SH in terms of its: a) annual and interannual variability and trend, and b) deviations with respect to our center's SH values (JPL-RO). The time series represent monthly zonal averages of the SH at individual pressure levels from the lower up to the middle troposphere: 700 hPa, 600 hPa, 500 hPa, and 400 hPa. We do not extend our analysis at higher altitudes due to the small contribution of water vapor on to the RO observations.

264 The latitude belt within $\pm 15^\circ$ encompasses the ascending branch of the Hadley cell
 265 circulation. Near to the surface, moist air masses from both hemispheres converge within this
 266 narrow equatorial region, collide, and lead to heavy precipitation. The amount of the latent heat
 267 released during rainfall warms the air driving strong rising motions, deep convection, and high
 268 cloud formation.
 269



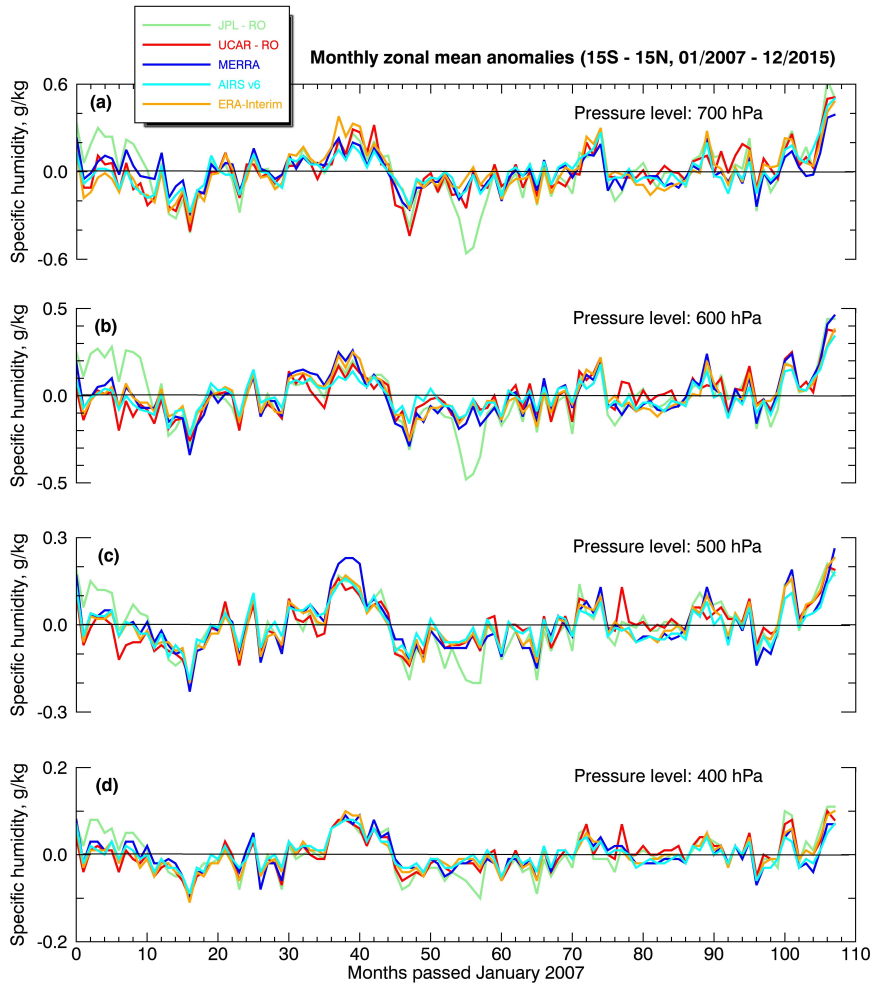
270
 271 **Figure 1.** Times series of the monthly zonal averages of the specific humidity from January 1,
 272 2007 until December 31, 2015 from JPL (green), UCAR (red), ERA-Interim (orange), MERRA
 273 (blue) and AIRS (cyan) at (a) 500 hPa, (b) 400 hPa, (c) 700 hPa, and (d) 600 hPa pressure levels.

274 Figure 1 shows the monthly zonal mean specific humidity as a function of time from
 275 January 2007 until December 2015 from 700 hPa up to 400 hPa. Qualitatively, all data sets
 276 capture the same variability pattern, exhibiting clear signatures of an annual and interannual
 277 cycle at all pressure levels. Quantitatively, the magnitude of the specific humidity varies among
 278 data sets having a minimum value of 5.0 g kg⁻¹ (summer and winter) and a maximum value of
 279 6.5 g kg⁻¹ (spring and autumn) at 700 hPa. Its value decreases with altitude and at 400 hPa
 280 fluctuates between 0.7 g kg⁻¹ (during summer and winter) and 1.0 g kg⁻¹ (during spring and
 281 autumn). Table 1 shows that the 9-year mean differences among all climatologies are < 20%,
 282 falling within the level of retrieval uncertainty of individual RO specific humidity profiles.
 283

284 **Table 1.** Mean climatology, deviation of the mean climatology from JPL, and linear regression
 285 fits of the specific humidity time series from JPL, UCAR, ERA–Interim, MERRA, and AIRS
 286 over the ±15° climate region. The 2-sigma uncertainties are estimated for each statistical metric,
 287 and their statistical significance is evaluated at p < 0.05 confidence level. Boxes filled with red
 288 are statistically insignificant.

PART I: 9-year long mean of specific humidity climatology with 2-sigma uncertainty, g kg ⁻¹					
Data Records	JPL	UCAR	ERA–Interim	MERRA	AIRS
400 hPa	0.99 ± 0.12	0.92 ± 0.10	0.94 ± 0.12	0.91 ± 0.10	0.81 ± 0.08
500 hPa	2.18 ± 0.26	2.01 ± 0.22	2.04 ± 0.22	2.08 ± 0.26	1.88 ± 0.20
600 hPa	3.88 ± 0.44	3.51 ± 0.30	3.62 ± 0.30	4.03 ± 0.44	3.55 ± 0.32
700 hPa	5.95 ± 0.60	5.64 ± 0.52	5.74 ± 0.46	5.99 ± 0.46	5.64 ± 0.44
PART II: 9-year long mean of specific humidity deviations from JPL–RO, g kg ⁻¹					
400 hPa	n/a	- 0.08	- 0.06	- 0.08	- 0.19
500 hPa	n/a	- 0.17	- 0.14	- 0.10	- 0.31
600 hPa	n/a	- 0.37	- 0.27	+ 0.15	- 0.33
700 hPa	n/a	- 0.31	- 0.22	+ 0.04	- 0.32
PART III: Linear regression of specific humidity anomalies with 2-sigma uncertainty, g kg ⁻¹ month ⁻¹					
400 hPa	(1.0±3.0)×10 ⁻⁴	(3.7±2.2)×10 ⁻⁴	(2.4±2.2)×10 ⁻⁴	(0.1±2.1)×10 ⁻⁴	(0.3±2.0)×10 ⁻⁴
500 hPa	(2.3±6.0)×10 ⁻⁴	(9.6±4.4)×10 ⁻⁴	(6.2±4.6)×10 ⁻⁴	(3.3±5.4)×10 ⁻⁴	(2.1±4.2)×10 ⁻⁴
600 hPa	(-1.8±10)×10 ⁻⁴	(15.1±6.6)×10 ⁻⁴	(6.3±6.8)×10 ⁻⁴	(8.4±8.0)×10 ⁻⁴	(6.3±5.4)×10 ⁻⁴
700 hPa	(6.1±12)×10 ⁻⁴	(17.2±9.0)×10 ⁻⁴	(14.1±8.8)×10 ⁻⁴	(1.3±7.2)×10 ⁻⁴	(12.9±7.2)×10 ⁻⁴

289 Due to averaging over 9 years, random and systematic errors in the time series are
290 significantly reduced, representing the degree of disagreement among climatologies. Despite
291 these differences, figure 2 shows that all interannual anomaly climatologies not only capture the
292 same variability patterns but they also have almost similar magnitudes. Their amplitude
293 fluctuates around $\pm 0.4 \text{ g kg}^{-1}$ at 700 hPa and decreases with altitude to $\pm 0.1 \text{ g kg}^{-1}$ at 400 hPa.



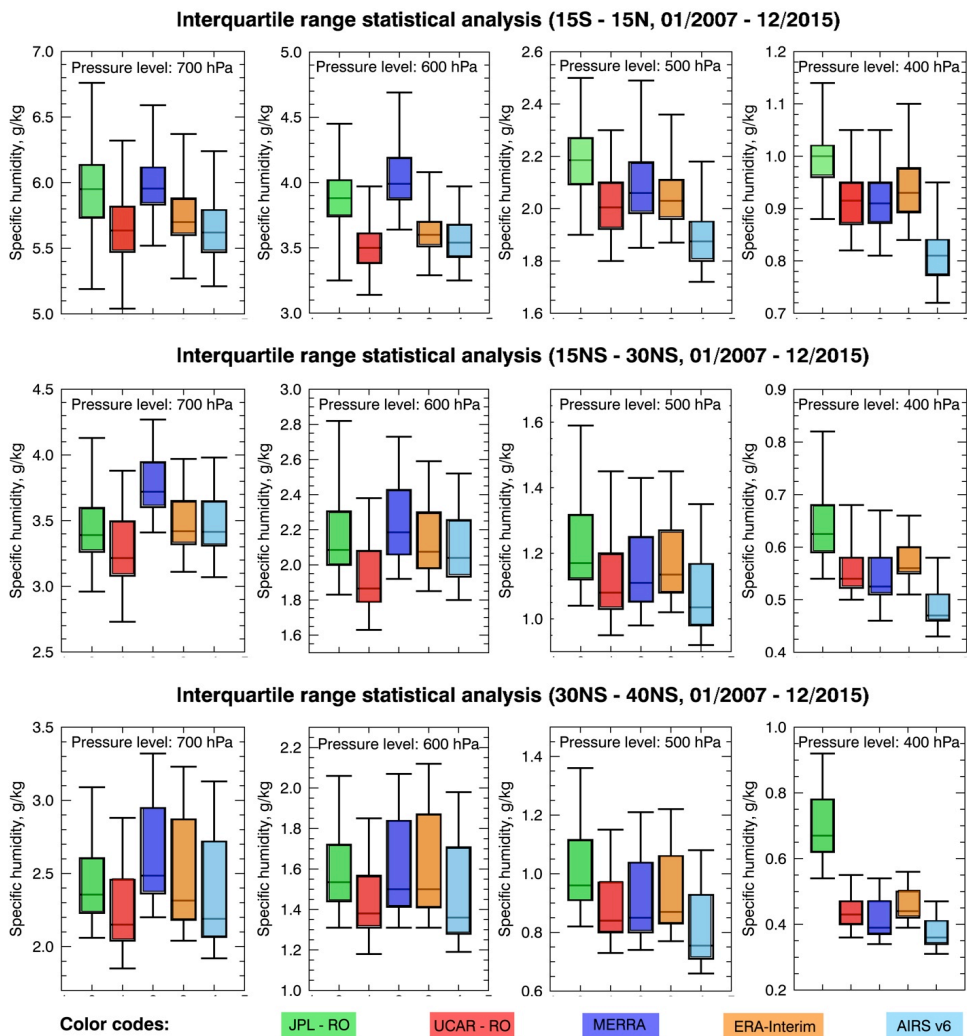
294
295 **Figure 2.** This is the same as figure 1, but for the specific humidity interannual anomalies.

296 During the strong La Niña event in 2010–2011 all interannual anomaly climatologies
297 captured an enhancement in specific humidity with respect to the background, which is more
298 pronounced at 500 hPa and 400 hPa marking the highest values in the time series. An even
299 stronger El Niño event occurred in 2015–2016 and the interannual anomalies in all climatologies
300 also started showing a pronounced increase in specific humidity. Interestingly, during the strong
301 La Niña event in 2007–2008, only the JPL climatology displayed increased specific humidity
302 values compared to the rest of the rest climatologies. The interannual anomaly variations for all
303 data sets in the middle troposphere correlate strongly (> 0.8) with those in the lower troposphere,
304 but have smaller amplitude.

305 A linear regression fit and a Student t -test on the specific humidity interannual anomalies
306 shows that the JPL and MERRA series do not suggest an increase in specific humidity with time
307 between 700 hPa and 400 hPa (cf., Table 1). However, the UCAR and ERA–Interim data sets,
308 show an increase of the tropospheric specific humidity, with slower increase rate with increasing
309 altitude. The difference between the two data sets is that UCAR–RO suggests faster moistening
310 of the troposphere than ERA–Interim. The AIRS data sets also show an increase of the specific
311 humidity at 700 hPa and 600 hPa at a rate similar to that of ERA–Interim, but no SH increase at
312 500 hPa and above.

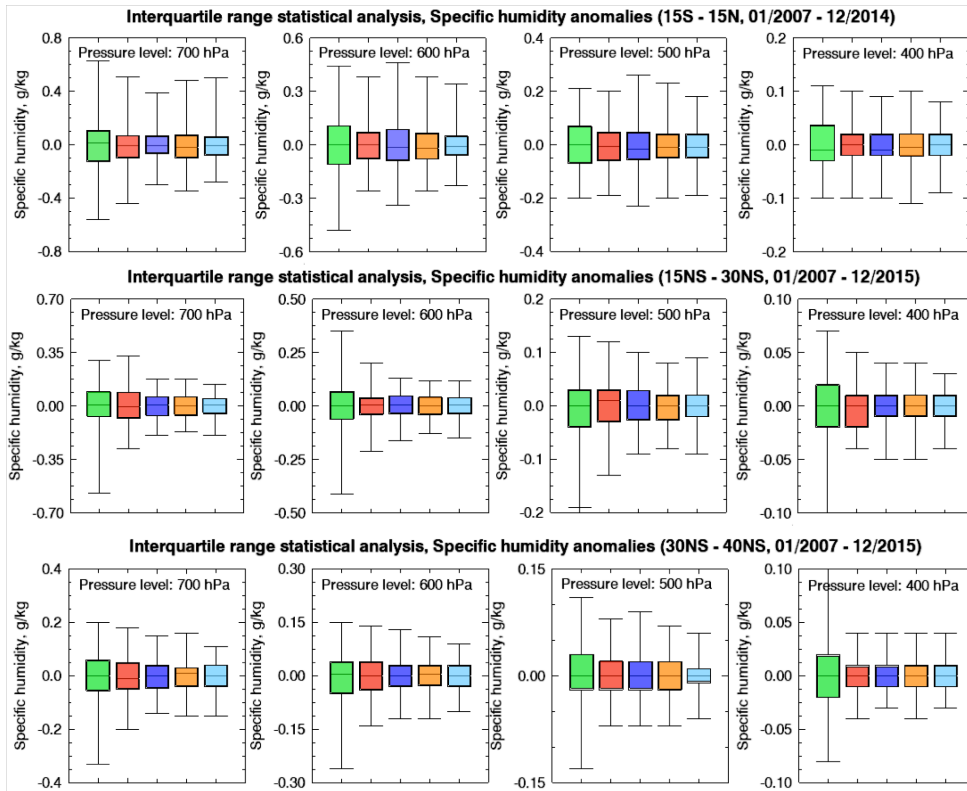
313 We statistically analyze the 9-year time series of the absolute specific humidity (cf.,
314 figure 1) and interannual anomaly climatologies (cf., figure 2) by estimating their respective
315 interquartile ranges as shown in figures 3 and 4. In these box plots, the solid black line inside the
316 boxes represents the median value of the 9-year climatologies. The length of the box represents
317 the value range within which we find 50% of the values around the median. The top and bottom
318 whiskers define the largest and the lowest monthly zonal mean values of the time series.

- Deleted: we find
- Deleted: suggest
- Deleted: the amount of SH
- Deleted: Contrary to that,
- Deleted: indicate a gradual increase of the absolute amount of SH throughout the vertical extend of the troposphere
- Deleted: . The increase is faster at 700 hPa and slows down
- Deleted: height
- Deleted: with
- Deleted: systematically indicating
- Deleted: SH



332

333 **Figure 3.** Boxplots of the monthly zonal mean specific humidity throughout the 2007–2015 time
 334 period for the 700 hPa, 600 hPa, 500 hPa, and 400 hPa over the ascending branch of Hadley cell
 335 ($\pm 15^\circ$) (top row), the trade winds belt ($\pm 15\text{--}30^\circ\text{NS}$) (middle), and the descending branch of
 336 Hadley cell at the subtropics ($\pm 30\text{--}40^\circ$) from JPL (green), UCAR (red), MERRA (blue), ERA–
 337 Interim (orange), and AIRS (cyan).



338

339 Figure 4. This is the same as figure 3, but for the specific humidity interannual anomalies.

340

341 ~~The top row in figure 1 presents statistical information about the median, the interquartile range~~

342 ~~(IQR), and the minimum and maximum values of the specific humidity time series over the~~

343 ~~entire observational record for all data sets throughout the vertical extent of the troposphere.~~

344 ~~Figure 2 shows details about the variability of the monthly zonal mean SH and Table 1~~

345 ~~summarizes the results of figure 2.~~

346 Figure 3 shows that in the lower troposphere, above the planetary boundary layer, the JPL

347 and MERRA products show almost the same median value of $\sim 6.0 \text{ g kg}^{-1}$ (at 700 hPa) and $\sim 4.0 \text{ g}$

Comment [15]:

Reviewer #2. Minor Comment #14.

Addressed and completed.

348 kg^{-1} (at 600 hPa). Their difference is $< 1.0\%$ and $< 4.0\%$ at 700 hPa and 600 hPa, respectively
349 (cf., Table 1) marking their excellent agreement. The UCAR, AIRS, and ERA–Interim data sets
350 are in a very good agreement with one another differing by $< 3.0\%$, and they are drier than the
351 JPL and MERRA products by $\sim 7.0\text{--}10\%$. This dryness is more pronounced at 600 hPa. In the
352 middle troposphere, at 500 hPa and 400 hPa, the MERRA, ERA–Interim, and UCAR
353 climatologies start agreeing very well with each other capturing 2.0 g kg^{-1} at 500 hPa and 0.9 g
354 kg^{-1} at 400 hPa. JPL appears to be the moistest of all data sets by $< 10\%$, whereas AIRS is the
355 driest of all data sets by $\sim 15\text{--}25\%$ and its dryness is more apparent at 400 hPa.

356 Figure 4 summarizes the statistics of all specific humidity interannual anomaly
357 climatologies. Despite the differences in the absolute values, the interannual anomalies: a) have
358 almost the same median value, b) have similar IQRs, and c) exhibit similar scattering around the
359 median with almost the same maximum and minimum values. This behavior is seen at 700 hPa
360 up to 400 hPa, with the scattering around the median to be more consistent among the
361 climatologies at higher altitudes. We should point out that the pronounced AIRS dry bias over
362 the deep tropics ITCZ [Hearty *et al.* 2014], due to sampling limitations over cloud-covered
363 regions, can explain the observed systematic lower specific humidity values with respect to all
364 data sets from 700 hPa up to 400 hPa. This suggests that IR observations over deep convective
365 environments do not properly capture the amount of water vapor in the atmosphere.

366 ~~ERA Interim underestimates the total cloud fraction over the $\pm 15^\circ$ region compared to~~
367 ~~MERRA [Dolinar *et al.*, 2016; figure 1] and is also colder than MERRA by 1.0 K in the 2006–~~
368 ~~2011 time period at the tropics at 700 hPa [Simmons *et al.*, 2014; figure 18]. Given the definition~~
369 ~~of specific humidity (as the product between the relative humidity and the saturation vapor~~
370 ~~pressure), it is evident why MERRA shows a wetter air than ERA Interim in the lower~~

371 ~~troposphere. However, the cold bias in the ERA Interim becomes small with altitude and~~
372 ~~reduces to almost zero at 500 hPa, and ERA Interim starts showing a warm bias with respect to~~
373 ~~MERRA at 300 hPa by 0.1–0.3 K [Simmons et al., 2014]. This temperature bias between the~~
374 ~~two reanalyses could possibly explain why the two reanalyses begin to estimate similar SH~~
375 ~~values at 500 hPa and 400 hPa.~~

Comment [16]:

Note: We decided to remove this detail, because this manuscript does not focus on the differences between the re-analyses.

377 3.2. Analysis of the specific humidity at the trade winds zones

378 The $\pm 15\text{--}30^\circ$ latitudinal belt, in both hemispheres, defines the trade winds zones, where
379 dry air masses descending from the Hadley cell at the subtropics travel towards the equator.
380 These regions exhibit shallower convection compared to the deep tropics, as clouds forming in
381 these regions are typically cumulus and do not extend above 4.0 km.

382 Figures S1 and S2 (cf., supplementary material) show that the specific humidity
383 climatology and the respective interannual anomaly for all data sets capture distinct annual and
384 interannual variability patterns at all pressure levels. The specific humidity is lower in the trade
385 winds zone than in the deep tropics ranging from 2.5–4.5 g kg⁻¹ at 700 hPa to 0.45–0.75 g kg⁻¹ at
386 400 hPa and the amplitude of the interannual anomalies is ~50% smaller in the 700–400 hPa
387 pressure range. The interannual anomalies are also correlated between 700 hPa and 400 hPa (>
388 0.6), but their degree of correlation is weaker than that over the deep tropics, and we do not
389 observe enhanced values during the strong La Niña and El Niño events as we observe over the
390 deep tropics. We suggest that this may be due to weaker convection over the trade winds zone
391 compared to the deep tropics; thus, establishing a weaker vertical connection. In the trade winds
392 zone, all data sets do not suggest a statistically significant increase in specific humidity (cf.,
393 Table S1), but we ought to point out that the linear regression fit slopes are negative.

394 Table S1 shows that the mean differences of the specific humidity over the 9-year period,
395 between JPL and the rest of the data sets, is smaller at 700 hPa, 600 hPa, and 500 hPa than the
396 differences in the deep tropics, except at 400 hPa where it remains almost the same. These
397 differences are smaller than 20% and fall within the retrieval uncertainty of the data sets. It
398 appears that over less convective regions the climatologies agree better with one another
399 suggesting that convection could may be a limiting factor in properly sensing the amount of
400 water vapor in the atmosphere.

401 Figure 3 (middle row) and figure S1 show that the specific humidity climatologies in the
402 trade winds zone have similar characteristics with the deep tropics at 500 hPa and 400 hPa. The
403 JPL data set appears to be again the wettest and the AIRS the driest compared to all
404 climatologies, whereas UCAR, ERA-Interim, and MERRA show a very good agreement in
405 between. The reason JPL appears to be the wettest at 500 hPa is because the summer season in
406 all years is wetter by ~4.0% than the rest of the data sets, but this difference is within the
407 systematic uncertainty of the retrievals. However, at 700 hPa and 600 hPa, we notice a different
408 behavior in terms of the data sets' agreement compared to our analysis in the deep tropics.
409 Specifically, the JPL, ERA-Interim, and AIRS data sets agree very well with one another having
410 differences of ~ 1.0% (at 700 hPa) and ~ 2.0–3.0% (at 600 hPa); but, these differences are
411 statistically insignificant. UCAR is the driest of all data sets by ~15% (with respect to MERRA)
412 and ~ 5.0–10% (with respect to JPL), and MERRA seems to overestimate the specific humidity
413 particularly at 700 hPa.

414 Figure 4 (middle row) and figure S2 show that the specific humidity interannual
415 anomalies are in excellent agreement with one another having almost the same median value,
416 similar IQR, and exhibit similar scattering around the median. The exception is the JPL

417 | climatology, which shows larger scattering towards negative anomaly values. This could be due
418 | to outliers in the data, which push down the lowest negative value. This behavior is seen at 700
419 | hPa up to 400 hPa and unlike the deep tropics, we do not observe enhanced specific humidity
420 | anomaly values in the climatologies during the strong La Niña and El Niño events (Figure S2).

421

422 | 3.3. Analysis of the **specific humidity** at the subtropics

423 | The $\pm 30\text{--}40^\circ$ latitude belt, in both hemispheres, defines the subtropics where dry air
424 | descends from the Hadley cell. These moderate-to-strong subsidence regions exhibit low cloud
425 | formation (especially during the summer months), while favoring formation of low-altitude
426 | marine boundary layer (MBL) clouds.

427 | Figures S3 and S4 (cf., supplementary material) show that the specific humidity
428 | climatology shows a distinct annual cycle signature at all pressure levels, with lower values
429 | $\sim 2.0\text{--}3.5\text{ g kg}^{-1}$ at 700 hPa to $0.3\text{--}0.6\text{ g kg}^{-1}$ at 400 hPa (except for the JPL climatology that
430 | appears wet biased) than the trade winds zones and the deep tropics. The amplitudes of the
431 | specific humidity interannual anomalies are also smaller by $\sim 50\%$ (cf., figure S8) than those
432 | estimated over the trade winds zone and the deep tropics. The specific humidity interannual
433 | anomalies show the same degree of correlation (~ 0.65) with altitude as the one estimated in the
434 | trade winds zones, suggesting again that the strength of the convection defines the correlation
435 | strength of the specific humidity anomalies throughout the vertical extent of the troposphere.
436 | Table S2 shows that ERA–Interim and UCAR (at all pressure levels) as well as AIRS (at 500
437 | hPa and 400 hPa) capture a moistening of the subtropics, except from the AIRS at 700 hPa and
438 | 600 hPa pressure levels where the data set indicates a decrease in the SH over time. JPL does not
439 | show a decrease/increase of specific humidity with time, and MERRA shows moistening of the

Comment [17]:

Reviewer #1. Specific Comment #8.

Addressed and completed.

440 middle troposphere. Compared to the deep tropics and the trade winds zones, [Table S2 shows](#)
441 [that the mean](#) differences of the specific humidity values between JPL and the rest of the data
442 sets are smaller than in the deep tropics and similar to the trade winds zone, except at the 400
443 hPa where it remains almost the same. Again, this hints towards the notion that different data sets
444 agree better with one another over regions characterized by less convection.

445 [Figure 3 \(bottom row\) and figure S3 show that the specific humidity climatologies in the](#)
446 [subtropics in the middle troposphere show the exact same behavior as in the deep tropics and the](#)
447 [trade winds zone at all pressure levels. Specifically, JPL captures moister air than all other data](#)
448 [sets](#) and this wetness is more pronounced at 400 hPa. [The AIRS is systematically the driest](#)
449 [among all climatologies, and MERRA, ERA-Interim, and UCAR show an excellent agreement](#)
450 [being in between the JPL and the AIRS data sets. At 700 hPa, MERRA and UCAR are the](#)
451 [wettest and driest climatologies respectively, with JPL, ERA-Interim, and AIRS having a very](#)
452 [good agreement lying in between. At 600 hPa, JPL agrees very well with both reanalyses](#)
453 [differing by < 2.0%, and UCAR agrees very well with AIRS being drier than by ~7.0%. All](#)
454 [these differences are smaller than each data set's retrieval uncertainty, except that of JPL at 400](#)
455 [hPa which is > 30%. Similar to the deep tropics and the trade winds zone, the specific humidity](#)
456 [interannual anomalies in the subtropics exhibit the same behaviors being in excellent agreement](#)
457 [with one another having almost the same median value, similar IQR, and similar scattering](#)
458 [around the median \(cf., figure 4 – bottom row and figure S8\).](#)

460 **3.4. Differences between JPL and UCAR specific humidity retrievals**

461 [To begin establishing the RO-derived specific humidity as a climate product, we must](#)
462 [investigate the origin of the observed differences between the JPL and UCAR specific humidity](#)

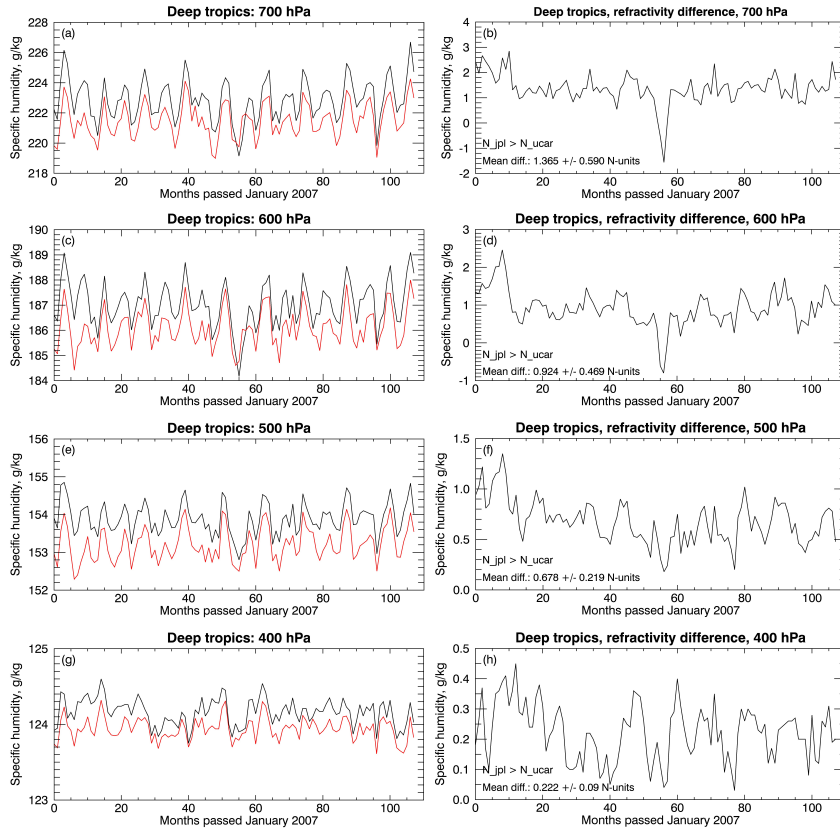
Comment [18]:

Reviewer #1. General Comment #2.

Reviewer #2. Minor Comment #13.

Addressed and completed.

463 [statistics. One of the possible reasons for the observed discrepancies in figure 1 could be the](#)
464 [difference in the refractivity products generated by each center. Here, we investigate this](#)
465 [possibility by analyzing the JPL and UCAR refractivity climatologies in the deep tropics.](#)
466



467
468 [Figure 5. Times series of the monthly zonal averages of the refractivity from January 1, 2007](#)
469 [until December 31, 2015 in the deep tropics \(\$\pm 15^\circ\$ \) from JPL \(black\) and UCAR \(red\) at \(a\) 700](#)
470 [hPa, \(b\) 600 hPa, \(c\) 500 hPa, and \(d\) 400 hPa pressure levels. The time series of the refractivity](#)
471 [differences between JPL minus UCAR are shown at \(e\) 700 hPa, \(f\) 600 hPa, \(g\) 500 hPa, and](#)
472 [\(h\) 400 hPa.](#)

473 Figure 5 shows that the monthly zonal averages of the JPL-derived refractivity are
474 systematically larger than those estimated by UCAR and this is noticeable at all pressure levels.
475 The JPL and UCAR climatologies are in excellent agreement, which becomes better with
476 increasing altitude. Interestingly, we notice a sharp dip in the JPL refractivity in figure 5 during
477 the summer of 2011 at 700 hPa and 600 hPa, which explains the JPL specific humidity
478 interannual anomaly dip during the same period at 700 hPa and 600 hPa in figure 2.
479 Quantitatively, the 9-year mean differences are 1.365±0.590 N-units (or 0.6% with respect to
480 UCAR) at 700 hPa, 0.924±0.469 N-units (or 0.5% with respect to UCAR) at 600 hPa,
481 0.678±0.217 N-units (or 0.4% with respect to UCAR) at 500 hPa, and 0.222±0.09 N-units (or
482 0.2% with respect to UCAR) at 400 hPa. From equation (1), we can derive an expression that
483 relates refractivity changes into water vapor pressure changes, assuming a constant temperature:

$$484 \delta N \equiv (N' - N) = a \cdot \frac{P}{T} + b \cdot \frac{(e + \delta e)}{T^2} - a \cdot \frac{P}{T} - b \cdot \frac{e}{T^2} = \frac{b}{T^2} \cdot \delta e \Leftrightarrow \frac{\delta N}{\delta e} = \frac{b}{T^2} \quad [3]$$

485
486 Where δN and δe represent the refractivity and water vapor pressure changes. We convert these
487 water vapor changes into specific humidity changes using equation (2). The mean refractivity
488 differences from figure 5 correspond to specific humidity differences of the order of: a)
489 0.26±0.11 g kg⁻¹ at 700 hPa, b) 0.19±0.10 g kg⁻¹ at 600 hPa, c) 0.16±0.05 g kg⁻¹ at 500 hPa, and
490 d) 0.06±0.02 g kg⁻¹ at 400 hPa. Comparing these values with the mean differences in Table 1, we
491 argue that the majority of the specific humidity differences between JPL and UCAR at all
492 pressure levels results from the refractivity differences between the two centers.

493 Another factor that could cause the JPL and UCAR specific humidity climatologies to
494 deviate is the different retrieval approaches adopted by JPL and UCAR. JPL uses equation (1) to

495 solve for the water vapor pressure by assuming a background temperature from the ECMWF
496 TOGA operational analysis. Comparisons of ECMWF operational products with rawinsondes
497 over the Pacific and Indian oceans reveal a systematic warm bias in the operational analysis of
498 the order of 0.5 K with an RMSE of 1.0 K [Nuret and Chong, 1996; Nagarajan and Aiyyer,
499 2004]. This bias leaks through the JPL retrievals, causing JPL to overestimate the specific
500 humidity (e.g., by $\sim 0.10 \text{ g kg}^{-1}$ at 500 hPa and 400 hPa). UCAR uses a variational assimilation
501 approach that takes ERA–Interim temperature and humidity information as *a-priori*. This could
502 explain why UCAR climatologies appear to be consistent with ERA–Interim at all altitudes in
503 the deep tropics and in the middle troposphere at the trade winds zone and the subtropics.
504 Additionally, the different quality control used by the two centers leads to a different number of
505 available occultations, which could also introduce a small bias in the specific humidity
506 comparisons. However, this effect would be small as we analyze monthly zonal averages.

508 4. Conclusions

509 Based on statistical tests using a 2-sigma uncertainty and 95% confidence level criteria
510 the RO observations agree very well with the MERRA, ERA-Interim, and AIRS climatologies
511 by capturing similar magnitudes and patterns of variability in the monthly zonal mean specific
512 humidity and interannual anomaly over annual and interannual timescales. The specific humidity
513 differences between RO and all other climatologies fall within the expected specific humidity
514 retrieval uncertainty. The JPL and UCAR specific humidity climatologies differ by less than
515 15% in the median (depending on location and pressure level) and these differences are primarily
516 due to the differences in the retrieved refractivity. Although we could explain these differences,
517 we cannot speculate which center is closer to the truth, we demonstrate that both JPL and UCAR

Comment [19]:

Reviewer #1. Specific Comment #6.

Addressed and completed.

Comment [20]:

Reviewer #1. General Comment #2.

Addressed and completed.

518 essentially provide similar specific humidity climatologies within the retrieval uncertainty. At
519 500 hPa and 400 hPa, in all climate zones, JPL appears to be the wettest of all data sets; AIRS is
520 the driest of all data sets, and UCAR, ERA-Interim, and MERRA are in very good agreement
521 lying in between the JPL and AIRS climatologies. In the lower-to-middle troposphere, we
522 present a complex behavior of discrepancies, as we speculate that this might be because the 700
523 hPa and 600 hPa pressure levels are closest to the planetary boundary layer that interfaces with
524 the free troposphere via convection and entrainment. This implies that the specific humidity
525 measured by each data set could be susceptible to the degree which each data set represents this
526 vertical coupling. Weather models are known to be less accurate over convective regions, and
527 recent studies indicate that RO observations could be positively biased by only 2% over cloudy
528 regions [Yang and Zou, 2017].
529 _____ Given the above, the RO observations could augment the reanalyses and satellite
530 observations by providing an independent additional complementary data set to study short-term
531 SH variations, which are critical to the study of water vapor trends, and climate sensitivity,
532 variability, and change. More detailed statistical analysis is required between the SH products
533 between different RO processing centers to define its structural uncertainty. The reduced daily
534 sampling of the COSMIC mission may be also a limiting factor in properly establishing
535 differences between the RO and other platforms. We expect that the increased sampling rate of
536 the COSMIC-2 follow-on mission will provide a much better picture of the tropical and
537 subtropical climatology, which will help us extend the current short-term RO record.

Comment [21]:

Reviewer #1. Specific Comment #9.

Addressed and completed.

Comment [22]:

Reviewer #1. Specific Comment #10.

Addressed and complete.

Comment [23]:

Reviewer #2. Minor Comment #15.

Addressed and completed.

Comment [24]:

Reviewer #2. Minor Comment #17.

Addressed and completed.

538

539

540

541 **Acknowledgments:**

542 This research was carried out at the Jet Propulsion Laboratory, California Institute of
543 Technology, under a contract with the National Aeronautics and Space Administration Earth
544 Science Mission Directorate (SMD). We thank Robert Khachikyan for making publicly available
545 the JPL-RO retrievals through the AGAPE interactive search tool. We would like to
546 acknowledge the University Corporation for Atmospheric Research (UCAR) COSMIC Data
547 Analysis and Archive Center (CDAAC) for making publicly available the COSMIC data sets.
548 We would like to thank NASA Earth Observing System Data and Information System (EOSDIS)
549 for making publicly available the MERRA and AIRS data sets. The RO SH products are publicly
550 available through JPL Global Environmental & Earth Science Information System (GENESIS)
551 portal at <ftp://genesis.jpl.nasa.gov/pub/genesis/glevels/cosmic?postproc>, as well as accessible via
552 the publicly available Atmospheric Grid Analysis and Extraction Profile (AGAPE) web interface
553 at <https://genesis.jpl.nasa.gov/agape/>. The AIRS/AMSU v6 Level-3 SH products are described in
554 detail in *Tian et al.* [2013], and for our analysis we use the AIRX3STM v006 data downloadable
555 from multiple different online tools, including the Simple Subset Wizard (SSW) at
556 <https://disc.gsfc.nasa.gov/SSW/> and the Mirador search base at <https://mirador.gsfc.nasa.gov>.
557 From the MERRA SH products we use are the MAIMNPANA v5.2.0 files, which we
558 downloaded from the SSW. The ERA-Interim SH products are publicly available at
559 <http://apps.ecmwf.int/datasets/data/interim-full-moda/levtype=sfc/>.

560
561
562
563

Comment [25]:
Reviewer #2. Minor Comment #10.
Addressed and completed.

564 **References:**

- 565 Anthes, R. A., et al. (2008), The COSMIC/FORMOSAT-3 mission: Early results, *Bull. Am.*
566 *Meteorol. Soc.*, **89**, pp. 313–333, doi:10.1175/BAMS-89-3-313
- 567 Ao, C. O., T. K. Meehan, G. A. Hajj, A. J. Mannucci, and G. Beyerle (2003), Lower troposphere
568 refractivity bias in GPS occultation retrievals, *J. Geophys. Res.*, **108**(D18), 4577,
569 doi:10.1029/2002JD003216
- 570 [Ao, C. O., D. E. Waliser, S. K. Chan, J.-L. Li, B. Tian, F. Xie, and A. J. Mannucci \(2012\),](#)
571 [Planetary boundary layer heights from GPS radio occultation refractivity and humidity](#)
572 [profiles, *J. Geophys. Res.*, **117**, D16117, doi:10.1029/2012JD017598](#)
- 573 Blackwell, W. J., M. Pieper, and L. G. Jairam (2008), Neural network estimation of atmospheric
574 profiles using AIRS/IASI/AMSU data in the presence of clouds, *Proc of SPIE*, 7149,
575 doi:10.1117/12.804841
- 576 [Bosilovich, M. G., F. R. Robertson, L. Takacs, A. Molod, and D. Mocko \(2017\), Atmospheric](#)
577 [Water Balance and Variability in the MERRA-2 Reanalysis, *J. Clim.*, **30**, pp. 1177–1196,](#)
578 [doi:10.1175/JCLI-D-16-0338.1](#)
- 579 Chen, J., A. D. Del Genio, B. E. Carlson, and M. G. Bosilovich (2008), The spatiotemporal
580 structure of twentieth-century climate variations in observations and reanalyses. Part I:
581 Long-term trend., *J. Clim.*, **21**, pp. 2611–2633, doi:10.1175/2007JCLI2011.1
- 582 Chuang, H., X. Huang, and K. Minschwaner (2010), Interannual variations of tropical upper
583 tropospheric humidity and tropical rainy-region SST: Comparisons between models,
584 reanalyses, and observations, *J. Geophys. Res.*, **115**, D21125,
585 doi:10.1029/2010JD014205
- 586 Collard, A. D., and S. B. Healy (2003), The combined impact of future space-based atmospheric

587 sounding instruments on numerical weather prediction analysis fields: A simulation
588 study, *Q. J. R. Meteorol. Soc.*, **129**, pp. 2741–2760

589 Dee, D. P., Uppala, S. M., Simmons, A. J., Berrisford, P., Poli, P., Kobayashi, S., Andrae, U.,
590 Balmaseda, M. A., Balsamo, G., Bauer, P., Bechtold, P., Beljaars, A. C. M., van de Berg,
591 L., Bidlot, J., Bormann, N., Delsol, C., Dragani, R., Fuentes, M., Geer, A. J., Haimberger,
592 L., Healy, S. B., Hersbach, H., Hólm, E. V., Isaksen, L., Kållberg, P., Köhler, M.,
593 Matricardi, M., McNally, A. P., Monge-Sanz, B. M., Morcrette, J.-J., Park, B.-K.,
594 Peubey, C., de Rosnay, P., Tavolato, C., Thépaut, J.-N. and Vitart, F. (2011), The ERA
595 Interim reanalysis: configuration and performance of the data assimilation system, *Q.J.R.*
596 *Meteorol. Soc.*, **137**, pp. 553–597. doi:10.1002/qj.828

597 Dolinar, E. K., X. Dong, and B. Xi (2016), Evaluation and intercomparison of clouds,
598 precipitation, and radiation budgets in recent reanalyses using satellite-surface
599 observations, *Clim. Dyn.*, **46**, pp. 2123–2144, doi: 10.1007/s00382-015-2693-z

600 Fasullo, J. T., and K. E. Trenberth (2012), A less cloudy future: The role of subtropical
601 subsidence in climate sensitivity, *Science*, **338**, pp. 792–794,
602 doi:10.1126/science1227465

603 Flato, G., J. Marotzke, B. Abiodun, P. Braconnot, S.C. Chou, W. Collins, P. Cox, F. Driouech,
604 S. Emori, V. Eyring, C. Forest, P. Gleckler, E. Guilyardi, C. Jakob, V. Kattsov, C.
605 Reason and M. Rummukainen, 2013: Evaluation of Climate Models. In: Climate Change
606 2013: The Physical Science Basis. Contribution of Working Group I to the Fifth
607 Assessment Report of the Intergovernmental Panel on Climate Change [Stocker, T.F., D.
608 Qin, G.-K. Plattner, M. Tignor, S.K. Allen, J. Boschung, A. Nauels, Y. Xia, V. Bex and
609 P.M. Midgley (eds.)]. Cambridge University Press, Cambridge, United Kingdom and

610 New York, NY, USA

611 Fetzer, E. J., B. H. Lambrigtsen, A. Eldering, H. H. Aumann, and M. T. Chahine (2006), Biases
612 in total precipitable water vapor climatologies from Atmospheric Infrared Sounder and
613 Advanced Microwave Scanning Radiometer, *J. Geophys. Res.*, **111**, D09S16,
614 doi:10.1029/2005JD006598

615 Fetzer, E. J., et al. (2008), Comparison of upper tropospheric water vapor observations from the
616 Microwave Limb Sounder and Atmospheric Infrared Sounder, *J. Geophys. Res.*, **113**,
617 D22110, doi:10.1029/2008JD010000

618 Frenkel, Y., A. J. Majda, and B. Khouider (2012), Using the Stochastic Multicloud Model
619 to Improve Tropical Convective Parameterization: A Paradigm Example, *J. Atmos.*
620 *Sci.*, **69**, pp. 1080–1105

621 Gorbunov, M. E., A. V. Shmakov, S. S. Leroy, and K. B. Lauritsen (2011), COSMIC Radio
622 Occultation Processing: Cross-Center Comparison and Validation, *J. Atmos. Oceanic*
623 *Technol.*, **28**, pp. 737–751, doi:http://dx.doi.org/10.1175/2011JTECHA1489.1

624 Hannay, C., et al. (2009), Evaluation of forecasted southeast Pacific stratocumulus in the NCAR,
625 GFDL, and ECMWF models, *J. Clim.*, **22**, pp. 2871–2889, doi:10.1175/2008JCLI2479.1

626 Hearty, T. J., A. Savtchenko, B. Tian, E. Fetzer, Y. L. Yung, M. Theobald, B. Vollmer, E.
627 Fishbein, and Y.-I. Won (2014), Estimating sampling biases and measurement
628 uncertainties of AIRS/AMSU-A temperature and water vapor observations using
629 MERRA reanalysis, *J. Geophys. Res. Atmos.*, **119**, pp. 2725–2741,
630 doi:10.1002/2013JD021205

631 Hegerl, G. *et al.* (2015), Challenges in quantifying changes in the global water cycle, *Bull. Amer.*
632 *Meteor. Soc.*, **96**, pp. 1097–1115

633 Ho, S.-P., Y.-H. Kuo, and S. Sokolovskiy (2007), Improvement of the temperature and moisture
634 retrievals in the lower troposphere using AIRS and GPS radio occultation measurements,
635 *J. Atmos. Oceanic Technol.*, **24**, pp. 1726–1737, doi:10.1175/JTECH2071.1

636 Ho, S.-P., X. Zhou, Y.-H. Kuo, D. Hunt, and J.-H. Wang (2010), Global Evaluation of
637 Radiosonde Water Vapor Systematic Biases using GPS Radio Occultation from COSMIC
638 and ECMWF Analysis, *Remote Sens*, **2**(5), pp. 1320-1330, doi:10.3390/rs2051320

639 Holloway, C. E., and J. D. Neelin (2009), Moisture vertical structure, column water vapor, and
640 tropical deep convection, *J. Atmos. Sci.*, **66**, pp. 1665–1683,
641 doi:http://dx.doi.org/10.1175/2008JAS2806.1

642 Jiang, J.H., et al. (2012), Evaluation of Cloud and Water Vapor Simulations in IPCC AR5
643 Climate Models Using NASA “A-Train” Satellite Observations, *J. Geophys. Res.*,
644 **117**, D14105, doi:10.1029/2011JD017237

645 Kahn, B. H., F. W. Irion, V. T. Dang, E. M. Manning, S. L. Nasiri, C. M. Naud, J. M. Blaisdell,
646 M. M. Schreier, Q. Yue, K. W. Bowman, E. J. Fetzer, G. C. Hulley, K. N. Liou, D.
647 Lubin, S. C. Ou, J. Susskind, Y. Takano, B. Tian, and J. R. Worden (2014), The
648 Atmospheric Infrared Sounder version 6 cloud products, *Atmos. Chem. Phys.*, **14**,
649 pp. 399–426, doi:https://doi.org/10.5194/acp-14-399-2014

650 Kishore, P., M. Venkat Ratnam, S. P. Namboothiri, I. Velicogna, G. Basha, J. H. Jiang,
651 K. Igarashi, S. V. B. Rao, and V. Sivakumar (2011), Global (50S–50N) distribution of
652 water vapor observed by COSMIC GPS RO: Comparison with GPS radiosonde, NCEP,
653 ERA Interim, and JRA-25 reanalysis datasets, *JASTP*, **73**(13), pp. 1849–1860

654 Kuo, Y.-H., W. S. Schreiner, J. Wang, D. L. Rossiter, and Y. Zhang (2005), Comparison of GPS
655 radio occultation soundings with radiosondes, *Geophys. Res. Lett.*, **32**, L05817,

656 doi:10.1029/2004GL021443

657 Kursinski, E. R., and T. Gebhardt (2014), A Method to Deconvolve Errors in GPS RO-Derived
658 Water Vapor Histograms, *J. Atmos. Ocean. Technol.*, **31**, pp. 2606–2628,
659 doi:10.1175/JTECH-D-13-00233.1

660 Kursinski, E. R., G. A. Hajj, J. T. Schofield, R. P. Linfield, and K. R. Hardy (1997), Observing
661 Earth's atmosphere with radio occultation measurements using the Global Positioning
662 System, *J. Geophys. Res.*, **102**(D19), pp. 23,429–23,465, doi:10.1029/97JD01569

663 Kursinski, E. R., and G. A. Hajj (2001), A comparison of water vapor derived from GPS
664 occultations and global weather analyses, *J. Geophys. Res.*, **106**(D1), pp. 1113–1138,
665 doi:10.1029/2000JD900421

666 [Nagarajan, B., and A. R. Aiyer \(2004\), Performance of the ECMWF Operational Analyses over](#)
667 [the Tropical Indian Ocean, *Mon. Weath. Rev.*, **132**, pp. 2275–2282,](#)
668 [doi:10.1175/1520-0493\(2004\)132<2275:POTEOA>2.0.CO;2](#)

669 [Nuret, M., and M. Chong \(1996\), Monitoring the performance of the ECMWF operational](#)
670 [analysis using the enhanced TOGA COARE observational network, *Wea. Forecasting*,](#)
671 [11, pp. 53–65, doi:10.1175/1520-0434\(1996\)011<0053:MTPOTE>2.0.CO;2](#)

672 Read, W. G., et al. (2007), Aura Microwave Limb Sounder upper tropospheric and lower
673 stratospheric H₂O and relative humidity with respect to ice validation, *J. Geophys.*
674 *Res.*, **112**, D24S35, doi:10.1029/2007JD008752

675 Rienecker, M. M., M. J. Suarez, R. Todling, J. Bacmeister, L. Takacs, H.-C. Liu, W. Gu,
676 M. Sienkiewicz, R. D. Koster, R. Gelaro, I. Stajner, and J.E. Nielsen (2008), The
677 GOES-5 Data Assimilation System – Documentation of versions 5.0.1, 5.1.0, and
678 5.2.0, *NASA Tech. Rep.*, Series on Global Modeling and Data Assimilation,

679 NASA/TM-2008-104606, **27**, 92 p.

680 Rienecker, M. M., and Coauthors (2011), MERRA: NASA's Modern-Era Retrospective
681 Analysis for Research and Applications. *J. Climate*, **24**, pp. 3624–3648,
682 doi: <http://dx.doi.org/10.1175/JCLI-D-11-00015.1>

683 Schreier, M. M., B. H. Kahn, K. Sušelj, J. Karlsson, S. C. Ou, Q. Yue, and S. L. Nasiri (2014),
684 Atmospheric parameters in a subtropical cloud regime transition derived by AIRS and
685 MODIS: observed statistical variability compared to ERA-Interim, *Atmos. Chem. Phys.*,
686 **14**, pp. 3573–3587

687 Sherwood, S. C., R. Roca, T. M. Weckwerth, and N. G. Andronova (2010), Tropospheric water
688 vapor, convection, and climate, *Rev. Geophys.*, **48**, RG2001,
689 doi:10.1029/2009RG000301

690 Simmons, A. J., and A. Hollingsworth (2002), Some aspects of the improvement in skill of
691 numerical prediction, *Q. J. R. Meteorol. Soc.*, **128**, pp. 647–677

692 Simmons, A. J., M. Hortal, G. Kelly, A. McNally, A. Untach, and S. Uppala (2005), ECMWF
693 analyses and forecasts of stratospheric winter polar vortex breakup: September 2002 in
694 the southern hemisphere and related events, *J. Atmos. Sci.*, **62**, pp.668–689

695 Simmons, A. J., Poli, P., Dee, D. P., Berrisford, P., Hersbach, H., Kobayashi, S. and Peubey, C.
696 (2014), Estimating low-frequency variability and trends in atmospheric temperature using
697 ERA-Interim, *Q. J. R. Meteorol. Soc.*, **140**, pp. 329–353, doi:10.1002/qj.2317

698 [Sokolovskiy, S., C. Rocken, D. Hunt, W. Schreiner, J. Johnson, D. Masters, and S. Esterhuizen](#)
699 [\(2006\), GPS profiling of the lower troposphere from space: Inversion and demodulation](#)
700 [of the open-loop radio occultation signals, *Geophys. Res. Lett.*, **33**, L14816,](#)
701 [doi:10.1029/2006GL026112](http://dx.doi.org/10.1029/2006GL026112)

702 [Takacs, L. L., M. Suarez, and R. Todling \(2016\), Maintaining atmospheric mass and water](#)
703 [balance in reanalyses, *Quart. J. Roy. Meteor. Soc.*, **142**, 1565–1573, doi:10.1002/qj.2763](#)

704 Tian, B., E. J. Fetzer, B. H. Kahn, J. Teixeira, E. Manning, and T. Hearty (2013), Evaluating
705 CMIP5 Models using AIRS Tropospheric Air Temperature and Specific Humidity
706 Climatology, *J. Geophys. Res. Atmos.*, **118**, 114–134, doi:10.1029/2012JD018607

707 Vergados, P., A. J. Mannucci, and C. O. Ao (2014), Assessing the performance of GPS radio
708 occultation measurements in retrieving tropospheric humidity in cloudiness: A
709 comparison study with radiosondes, ERA-Interim, and AIRS data sets, *J. Geophys. Res.*
710 *Atmos.*, **119**, pp. 7718–7731, doi:10.1002/2013JD021398

711 Vergados, P., A. J. Mannucci, C. O. Ao, J. H. Jiang, and H. Su (2015), On the comparisons of
712 tropical relative humidity in the lower and middle troposphere among COSMIC radio
713 occultations and MERRA and ECMWF data sets, *Atmos. Meas. Tech.*, **8**, pp. 1789–1797,
714 doi:<https://doi.org/10.5194/amt-8-1789-2015>

715 Wang, H., and W. Su (2013), Evaluating and understanding top of the atmosphere cloud
716 radiative effects in Intergovernmental Panel on Climate Change (IPCC) Fifth Assessment
717 Report (AR5) Coupled Model Intercomparison Project Phase 5 (CMIP5) models using
718 satellite observations, *J. Geophys. Res. Atmos.*, **118**, pp. 683–699,
719 doi:10.1029/2012JD018619

720 Wang, B. R., X.-Y. Liu, and J.-K. Wang (2013), Assessment of COSMIC radio occultation
721 retrieval product using global radiosonde data, *Atmos. Meas. Tech.*, **6**, pp. 1073–1083,
722 doi:10.5194/amt-6-1073-2013

723 Waters et al. (2006), The Earth Observing System Microwave Limb Sounder (EOS MLS) on the
724 Aura Satellite, *IEEE Trans. Geosci. Remote Sens.*, **44**, pp. 1075–1092

725 Wu, W.-S., R.J. Purser, and D.F. Parrish (2002), Three-dimensional variational analysis with
726 spatially inhomogeneous covariances, *Mon. Wea. Rev.*, **130**, pp. 2905–2916
727 [Xie, F., D. L. Wu, C. O. Ao, E. R. Kursinski, A. J. Mannucci, and S. Syndergaard \(2010\), Super](#)
728 [refraction effects on GPS radio occultation refractivity in marine boundary](#)
729 [layers, *Geophys. Res. Lett.*, **37**, L11805, doi:10.1029/2010GL043299](#)
730 [Yang, S. and X. Zou \(2017\), Dependence of positive refractivity bias of GPS RO cloudy profiles](#)
731 [on cloud fraction along GPS RO limb tracks, *GPS Solut.*, **21**, pp. 499–509,](#)
732 [doi:10.1007/s10291-016-0541-1](#)